Chapter 20

Application of Surface Plasmon Polaritons in CMOS Digital Imaging

Qin Chen, Xiaohua Shi, Yong Ma and Jin He

Additional information is available at the end of the chapter

http://dx.doi.org/10.5772/50757

1. Introduction

Recent years there has been a rapid expansion of research into nanophotonics based on surface plasmon polariton (SPP), which is a collective electron oscillation propagating along a metal-dielectric interface together with an electromagnetic wave [1]. What distinguishes SPPs from photons is that they have a much smaller wavelength at the same frequency. Therefore SPPs possess remarkable capabilities of concentrating light in a nanoscale and the resulted significant enhancement of localized field [2]. SPPs can be excited by an incident electromagnetic wave if their wavelength vectors match. This is usually achieved by nanopatterning the metal film. The resonant frequency of SPP is determined by the metal materials, dielectric materials, profiles and dimensions of the patterns, etc. As a result, the tunability of SPP enables its application as a colour filter in the visible range. Actually this was used in the stained glass manufacture hundreds years ago. Since the extraordinary optical transmission through a nanohole array in a thin metal film was reported by Ebbesen [3], the plasmonic photon sorting has been explored for the potential applications in digital imaging and light display [4,5]. In addition, SPP based light manipulating elements like planar metallic lenses, beam splitters, polarizers have been investigated both theoretically and experimentally [6-7].

In solid state digital imaging, complementary metal oxide semiconductor (CMOS) image sensors (CISs) are the leading mass-market technology. CMOS image sensors with smaller pixels are expected to enable digital imaging systems with better resolution and possibly high photosensitive area in the pixel (fill-factor). In present colour CMOS digital imaging systems, dye-doped polymer filters and curved dielectric microlenses are used to disperse light of different wavelengths and manipulate the light beams, respectively . With the down scaling of pixel size to the sub-2 μm range, these optical elements suffer from performance degradation, such as colour cross-talk, due to the large distance between the optical

elements and the photodiodes underneath [8]. Therefore most high-resolution digital cameras have to use the backside illuminated CISs that are fabricated with complicated processes [9]. Furthermore different colour polymer filters have to be fabricated successively in several process steps using the back-end-of-line process. Continuous development of new applications for CISs requires that they are able to be manufactured at low cost.

The idea of introducing plasmonics into a CIS was first proposed by Catrysse *et al* [10]. They were able to show the potential of metallic nanodevices in a CIS by detailed numerical simulations, and provided preliminary experimental results [10,11]. There are several advantages: (1) this technique has the potential to produce all the required colour filters in a single metal layer by one lithography step at a low cost; (2) colour cross-talk can be reduced by integrating plasmonic colour filters in Metal 1 layer which is very close to the CMOS photodiodes; (3) the thickness of the plasmonic device is one or two orders of magnitude thinner than that of the colourant one used in a CIS or a LCD; (4) localized field enhancement effect of metallic nanostructures may increase the photodetection sensitivity; (5) the light filtering can be readily obtained by varying the nanostructures that enables tuning of the resonant wavelengths and thus achieves a large spectral design freedom; (6) other optical elements such as lenses and polarizers can be achieved based on SPP in metal layers in CMOS technology. Planar metallic lenses integrated in the metal layers in standard CMOS technology can readily tune the phase of incident light on a pixel level to achieve a great control on the light beam divergence therefore the cross-talk especially for the pixels at the edge of the whole sensor; (7) plasmonic metal like aluminium is a CMOS compatible metal and it is more stable compared to polymer.

In this chapter, we briefly review the research progress on various plasmonic optical elements for the application in digital imaging and describe our work on a plasmonic CIS (pCIS). Section 2, 3 and 4 focus on plasmonic colour filters, PLs and wire-grid polarizers, respectively. Section 5 presents our work on the integration of plasmonic colour filters on CISs. Finally, we conclude this chapter and discuss the outlook of this technique.

2. Plasmonic colour filters

2.1. Background

A colour filter that selectively transmits or reflects input light is an important element in a CIS. Established colour filtering technologies for CISs use dye-doped polymers. Each colour filter for red (R), green (G) and blue (B) must be fabricated successively in several process steps. Because of the encroaching difficulties of cross-talk and the cost of manufacture, it is desirable to find new methods for building colour filters into CISs. Other colour filtering techniques for imaging arrays have been investigated. Guided-mode resonance filters based on subwavelength dielectric gratings were shown to work as a bandpass filter [12]. They can be designed to work in both reflection and transmission modes. Hybrid metal-dielectric gratings were found to offer excellent optical transmission (87%) property in the midinfrared range due to the Fano transmission resonance [13]. One-dimensional (1D)

periodic metal-insulator-metal (MIM) waveguide array supports a surface plasmon antisymmetric mode which showed colour filtering effect [14]. However, devices based on a 1D structure have an intrinsic polarization dependency. Photonic crystal colour filter was proposed for the application in a MOS image sensor, where two multilayer stack mirrors separated by a defect layer were used to form a cavity resulting a passband filtering [15]. But the dielectric mirrors have a relatively narrow bandwidth limited by the index contrast in the stack and the multilayer deposition process is complex. Silver mirrors were proposed to replace the dielectric mirrors and a CIS based on this technique was demonstrated where the different colours were achieved by tuning the cavity length [16]. The device requires multi-lithography steps to make R, G, B pixels. A bull's eye structure consisting of concentric grooves with a central hole was proposed as another candidate for colour filters [5]. This method gave very good narrow band wavelength filtering, but the low fill ratio resulted in poor transmission efficiency.

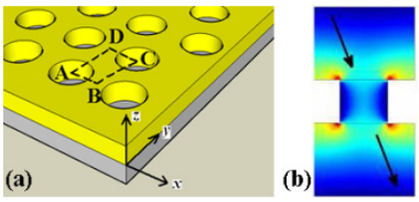

Figure 1. (a) A square-lattice hole array in a metal film. (b) Cross-section field distribution around a hole where light couples to SPPs.

Ebbeson *et al*. investigated the subwavelength holes in silver films as shown in Fig. 1(a) and observed extraordinary optical transmission (EOT) of light through the holes and wavelength filtering due to the excitation of surface plasmon resonance (SPR) [3]. The incident light first couples to the SPR at the top surface of the metal film in the presence of the 2D hole array. The SPR at the top surface then couples to the one at the bottom surface of the metal film. Finally, light reemits from the bottom surface of the patterned metal film as shown in Fig. 1(b). The peak position, λ_{max}, of the transmission spectrum at normal incidence can be approximated by

$$\lambda_{\max} = \frac{a}{\sqrt{i^2 + j^2}} \sqrt{\frac{\varepsilon_m \varepsilon_d}{\varepsilon_m + \varepsilon_d}} \quad (square \quad lattice) \tag{1}$$

$$\lambda_{\max} = \frac{a}{\sqrt{\frac{4}{3}(i^2 + ij + j^2)}} \sqrt{\frac{\varepsilon_m \varepsilon_d}{\varepsilon_m + \varepsilon_d}} \quad (triangular \quad lattice) \tag{2}$$

where a is the period of the array, ε_m and ε_d are the dielectric constants of the metal and the dielectric material in contact with the metal respectively, and i and j are the scattering orders of the array [3,4]. As shown in Eq. (1) and (2), the period determines the transmission peak positions of SPRs for a given material configuration. Following this discovery, researchers started to use 2D hole arrays in metal films as transmissive colour filters. A square-lattice

hole array surrounded by a square-lattice dimples at the same period in a silver film was reported to show colour filtering function [4]. Without surrounding dimples, a square array of circular holes were designed and fabricated in a thin aluminium film as red and green colour filters [17], where unfortunately the green filter devices exhibited a yellow colour due to the high colour cross-talk.

In this section, we focus on transmitted colour filters consisting of triangular-lattice hole arrays in aluminium films that are compatible with standard CMOS technology. Both numerical simulation and experimental results are presented.

2.2. FDTD simulation

Eq. (1) and (2) theoretically predict the resonant wavelengths of SPRs. But the thickness of the metal film and the coupling between the SPRs at two interfaces has not been considered in these equations. To accurately optimize the design, a finite-difference time-domain (FDTD) algorithm based commercial software, Lumerical FDTD Solutions [18], was used to investigate the colour filters and identify the transmission peaks in the measured spectra. As shown in Eq. (1) and (2), the wavelength interval between the first two SPR peaks in a triangular array is larger than that for a square array of a same period. Therefore we focus on the triangular lattice in the following part. In our work, we focus on a triangular-lattice hole array in an aluminium film on glass. Compared to silver and gold, aluminium is compatible with standard CMOS technology and cheap although it has a relatively higher absorption loss. Aluminium also has good adhesion to many substrates making fabrication easier.

The effects of the structure dimensions were investigated numerically. As shown in Fig. 2(a), the transmission efficiency was strongly affected by the size of the circular hole. As the hole size increases, the magnitude of the main transmission peak increases from 24% to 75%. There is also a red shift and an increase in the full-width at half-maximum (FWHM) from 60 nm to 300 nm. The reflections at the transmission peaks are almost zero in all three cases. Therefore the loss at the transmission peak is larger at a smaller radius, where the absorption within the metal due to the non-zero imaginary component of the permittivity increases [4]. A tradeoff between transmission and FWHM must be considered to optimize the RGB filters for the application in a CIS. The coupling between the SPRs at both sides of the metal film has an important effect on the transmission spectra. As shown in Fig. 2(b), the structure made with a thinner aluminium film has higher transmission but also a much larger bandwidth. The enhanced coupling of SPR in the case of a thin metal film increases the splitting of the two transmission peaks, i.e. the long wavelength side peak has a red shift but the short wavelength side peak has a blue shift. In addition, the transmittance of the very low level at a thickness of 30 nm. The EOT phenomenon is more prominent in the case of a thin metal film where the SPR coupling is strong. However, the FWHM is large for a thick metal film and may cause a spectral cross-talk for the RGB filters. Predicting in Eq. (2), the period has a dominant effect on the transmission peak, i.e. the transmitted colour of the filter. The filters shown in Fig. 2(c) have the peak transmissions around 50% filters in the visible range can be readily obtained by tuning the period of the hole array. Finally, the

different hole shapes with a similar area in a same triangular lattice were investigated as shown in Fig. 2(b). The circular hole array has the highest transmittance at the transmission peak and the smallest FWHM. Therefore, we focused on the circular hole array in our experiments. Plasmonic colour filters with spectral responses matching the International Commission on Illumination colour matching functions are useful for effectively communicating color between colour detection and output devices. A fully automated genetic algorithm that incorporated on-demand 3D FDTD simulations were used to determine the structure dimensions [19].

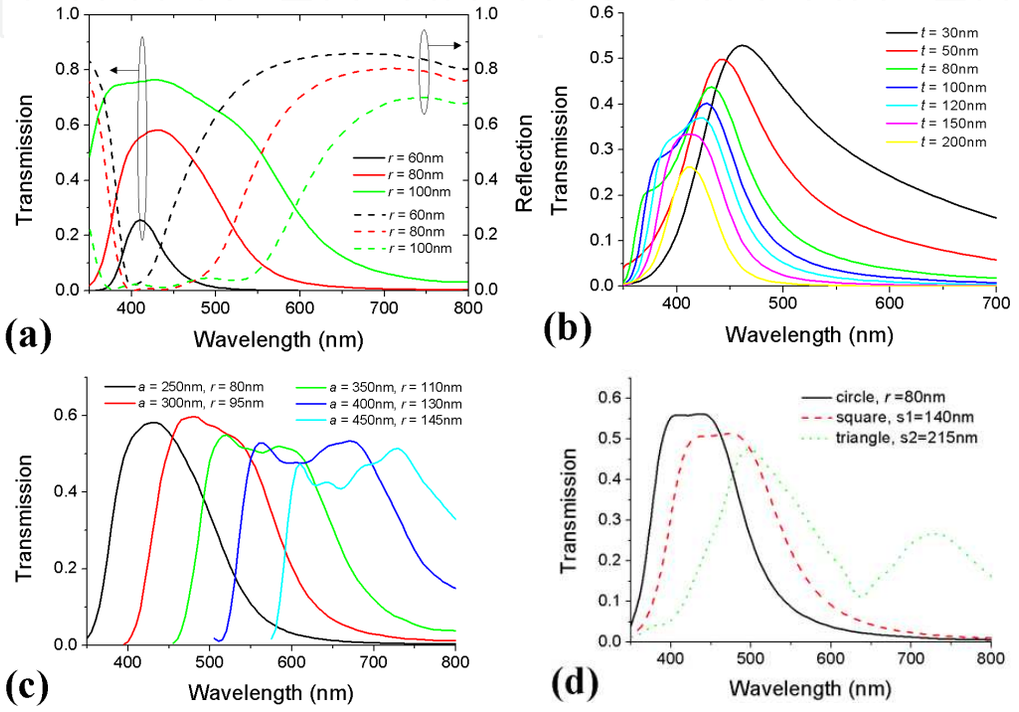

Figure 2. Simulated transmission/reflection spectra for hole arrays in a triangular lattice in an aluminium film on glass with a 200 nm SiO_2 cap layer. (a) Different circular hole radius r with a period a = 250 nm and a thickness t = 150 nm. (b) Different t at a = 250 nm and r = 65 nm. (c) Different a and r at t = 150 nm. (d) Different hole shapes.

2.3. Fabrication of colour filters on glass

Fig. 3(a) is the process flow for fabricating plasmonic colour filters. The first step is to evaporate a 150 nm aluminium film on a clean glass substrate at a rate of 0.3 nm/s by electron beam evaporation. Then ZEP520A electron beam resist was spin-coated on to the sample and exposed. After development, aluminium was etched using $SiCl_4$ in a Plasmalab System 100. Finally, a 200 nm SiO_2 layer is deposited on top of the patterned aluminium film after removal of the residual resist to enhance the transmission due to the symmetric SPR coupling (the refractive index of SiO_2 is close to that of glass). Fig. 3(b) shows a scanning electron microscope (SEM) image of patterned aluminium film after removing the residual resist. Vertical and smooth sidewalls can be seen from the inset SEM image for which the sample was tilted at 30º [20].

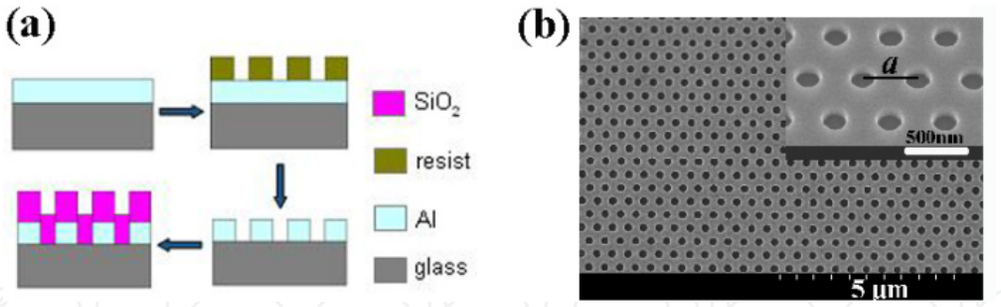

Figure 3. (a) Process flow for fabricating plasmonic colour filters. (b) A SEM image of etched holes in a triangular array with a = 430 nm in an aluminium film on glass. The inset is a SEM image for a sample tilted at 30º.

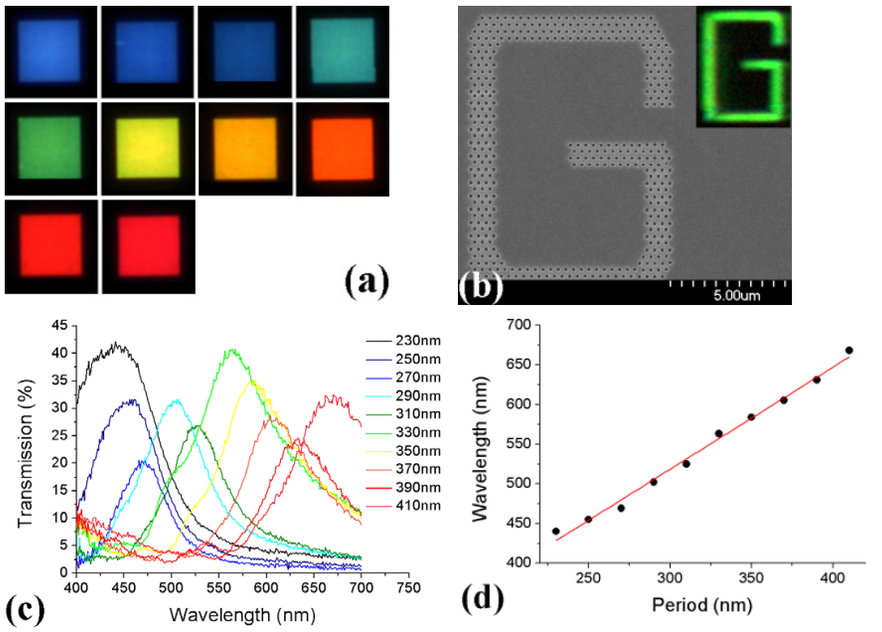

Figure 4. Performance of various plasmonic colour filters fabricated on glass. (a) Images of various plasmonic colour filters taken in microscope transmission mode under a white light illumination. (b) A SEM image of holes composing the letter 'G' with a = 330 nm. The transmitted light image of the structure with a 200 nm SiO_2 cap layer is shown in the inset. (c) Transmissive spectra of the filters shown in (a). (d) Wavelengths at which transmission through each peak versus the period of the plasmonic nanostructures. Reprint from [21].

The colour images of plasmonic filters were examined using an Olympus BX51 microscope fitted with a broadband halogen lamp. Fig. 4(a) shows the well-defined colour squares with a size of 50 μm × 50 μm consisting of holes in a triangular lattice with different periods. A letter 'G' consisting of holes with a = 330 nm was fabricated as shown in Fig. 4(b), where the period number of hole array is as small as three. The clear green letter 'G' appeared under the white light illumination as shown in the inset. Unlike the structures in earlier work [4], there is no dimple around the etched holes in our structure. This means that the pixel size could be as small as 1 μm on a high-resolution image sensor. Spectral measurement was carried out on a microscope spectrophotometer TFProbe MSP300 that can sample the signal from a minimum area of 10 μm × 10 μm. Different colour filters were

written on to the same sample to ensured consistent measurement of the different structures. Due to the symmetrical properties of the triangular-lattice hole array and the circular holes, the transmittance shows no difference for illumination at different polarization angles. An unpolarized light beam from a halogen lamp was launched normally on to the back-side of the sample. The transmitted light was collected using a 40× lens with a *NA*=0.9 and guided to the spectrometer and image camera. The transmission spectra from the sample in the visible range from 400 nm to 700 nm are shown in Fig. 4(c), where transmittances are between 20% and 40%, with full width at half maximum between 70 nm and 110 nm. As predicted in Eq. (2), Fig. 4(d) shows that the wavelength at which transmission through each filter peaks was found to linearly increase with the period of the holes. This means that a complete colour filter set can be reliably made using a single lithographic step.

3. Plasmonic polarizers

3.1. Background

Polarization is a general property of light and contains information about reflecting objects that traditional intensity-based sensors like human being's eyes ignore. However, polarization offers a number of advantages for imaging [22-24]. Polarization filtering has long been used in photography through haze. Difficult computer vision tasks such as image segmentation and object orientation are made tractable with polarization vision techniques. Investigation of the polarized light backscattering enables noninvasive surface and beneath-the-surface imaging of biological systems. Traditionally, the polarization image was obtained by taking an objective at the same place twice at different polarization angle with an external polarizer mounted in front of the camera. Mathematic analysis on these data finally generates a polarization image. Obviously, this method has low efficiency, low accuracy and high cost. Micropolarizer array was proposed to implement the polarization imaging like a Baye array in colour filter array [25,26]. In each 2×2 cell, there are four polarizers at different polarization angles to collect the required polarization information. Similar to a colour image, polarization image can be obtained from a polarization image sensor with micropolarizer arrays by just one shot of the scene. In the past, micropolarizer array was fabricated using polymer which is usually above 10 μm [25]. The large thickness causes large cross-talk between neighboring pixels. Furthermore, polymer polarizer faces a stability issue. Alternatively, metal wire grids are an ideal polarizer, which has been applied for IR polarization imaging [26]. Optimization of metal wire grids for a large extinction ratio (ER), defined as the transmission ratio of TM modes (the polarization of light perpendicular to the metal wire grid) to TE modes (the polarization of light parallel to the metal wire grid), is important to a high-contrast polarization image.

In this section, we numerically investigate the plasmonic polarzers and demonstrate the experimental results of aluminium grating polarizers.

3.2. Simulation

2D FDTD simulation is used to investigate the performance of metal wire grids. Wire grids with different periods were simulated and the results are shown in Fig. 5. In all cases, the effect. With the decreasing of the period, the transmission of TM polarization keeps at a high value but that of TE polarization decreases significantly. As a result, the ER increases with the decrease of the period. The state-of-the-art CMOS technology enables a feature size below 50 nm. However, a thick metal layer increases the aspect ratio of the gratings and therefore increases the difficulty in fabrication. The aspect ratio also affects the ER of the wire grids. As shown in Fig. 6, with a period of 100 nm, the transmission of TE polarization decreases more than one order of magnitude and the ER of Al wire grids increases approximately 15 dB when t increases 50 nm. All the above results are for wire grids with a duty cycle (metal filling ratio) of 50%. In Fig. 7, we show the effect of the duty cycle.

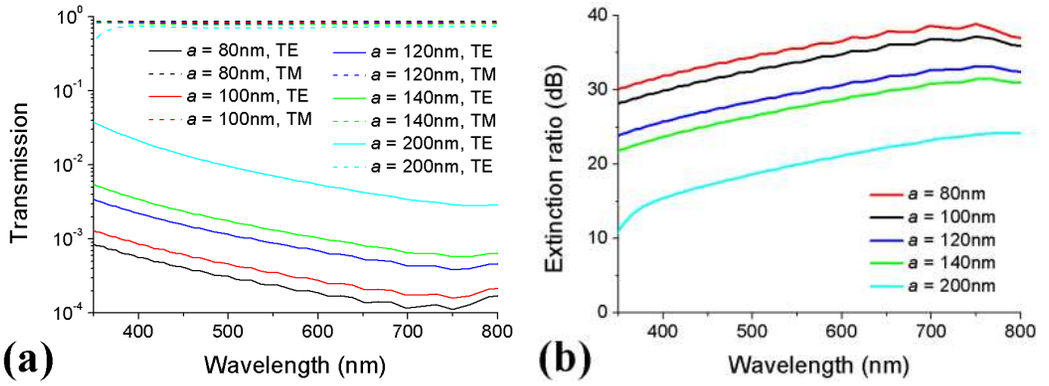

Figure 5. Transmission spectra (a) and ER (b) of Al wire grids on glass with different periods at t = 100 nm and f = 50%.

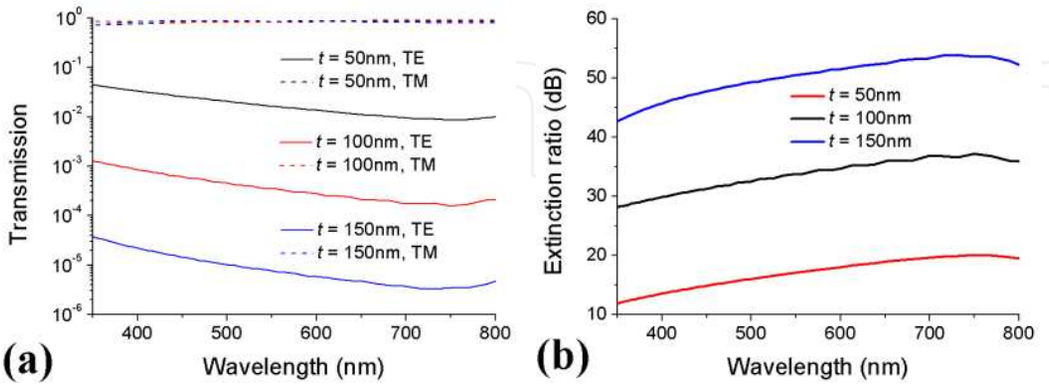

Figure 6. Transmission spectra (a) and ER (b) of Al wire grids on glass with different metal thicknesss at a = 100 nm and f = 50%.

Transmissions of both TE and TM polarizations reduce when the duty cycle increases. Furthermore, ER is higher at a higher duty cycle.

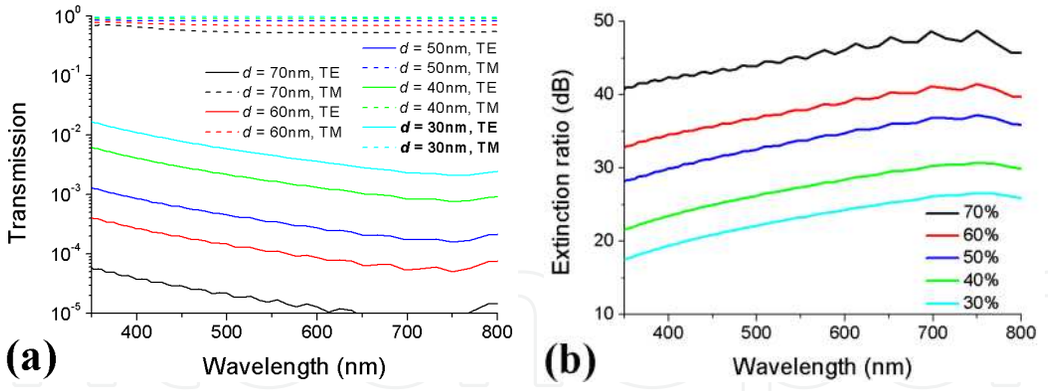

Figure 7. Transmission spectra (a) and ER (b) of Al wire grids on glass with different duty cycle at a = 100 nm and t = 100 nm.

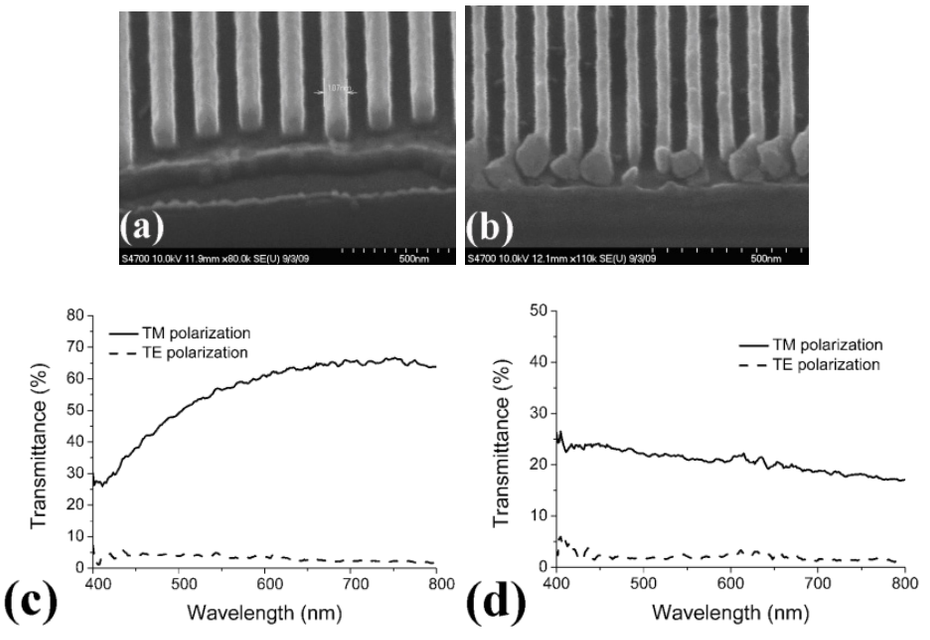

Figure 8. SEM images of fabricated Al wire grids with a period of 200 nm (a) and 100 nm (b). (c) and (d) Measured transmission spectra of polarizers in (a) and (b).

3.3. Experiments

The process flow is similar to that of plasmonic colour filters. The SEM images of devices with periods of 200 nm and 100 nm are shown in Fig. 8(a) and (b), respectively. Spectral measurement was carried out on a same microscope spectrophotometer TFProbe MSP300 as the plasmonic colour filter experiments. The incident light was polarized using a linear polarizer amounted before the sample in the light path. The transmitted light was collected using a 40× lens with a *NA*=0.9 and guided to the spectrometer. As the simulation results, the TM polarization has higher transmission than TE polarization as shown in Fig. 8(c) and (d). The measured ER of the device with a period of 100 nm is approximately 16, enabling a 4-bit polarization imaging. Actually, our polarizers may have better performance because the transmittance of TE polarization was closed to the

background noise limited by our detector. In addition, dual grating structures may be considered to obtain a higher ER [27].

4. Plasmonic Lenses (PLs)

4.1. Background

Traditionally light is manipulated using dielectric optical elements such as refractive lens, diffractive gratings, mirrors and prisms. For example, dielectric microlens arrays are used in current CMOS image sensor to increase the light collection efficiency. However, diffraction may put the usefulness of the microlens in question in sub-2μm pixels [28]. Recent progress in nanotechnology and the theory of plasmonics has led to rapidly growing interest in the implementation of metallic optical elements on a nano-scale for light beam manipulation [29-39]. Especially, lots of theoretical predictions [30-35] and experimental demonstration [28,36-39] have been reported on both one-dimensional (1D) and 2D PLs. However, most experimental results showed a large deviation of focal length from the design [28,36-39]. The authors attributed this phenomenon to the finite size of the lenses and the resulting diffraction. The effect of the lens size on the focal length was theoretically investigated in a plano-convex refractive microlens [40]. It turned out that the upper limit of the focal length was determined by the lens aperture due to the diffraction effect.

In this section, we discuss the diffraction effect in PLs and experimentally demonstrate PLs with accurate control of the focal lengths that are important for the application in a CIS.

4.2. Theory

A 1D PL, as shown in Fig. 9(a), is a group of nano-slits in metal that form zones to modulate the phase delay distribution across the device surface. It focuses light only in the x-direction. The distribution of the phase delay at the exit of each slit is designed to provide constructive interference at the focus. Incoming laser light excites SP modes at the slit entrances that propagate through the slits before emitting into light at the exits, forming a convergent focus. In general, the SP modes can be excited in a metal/dielectric/metal waveguide, as shown in the inset of Fig. 9(b), under TM-polarized illumination with the electric field perpendicular to the slits. In a narrow slit, only the fundamental SP mode exists with a complex propagation constant, β, that can be calculated from the equation

$$\tanh\left(\sqrt{\beta^2 - k_0^2\varepsilon_d}\,\frac{w}{2}\right) = \frac{-\varepsilon_d\sqrt{\beta^2 - k_0^2\varepsilon_m}}{\varepsilon_m\sqrt{\beta^2 - k_0^2\varepsilon_d}} \tag{3}$$

where ε_d and ε_m are the permittivity of the dielectric inside the slit and the metal, w is the slit width, and k_0 is the wave vector of light in free space [41]. The real and imaginary part of the effective refractive index n_{eff}, defined to be β/k_0, determine the phase velocity and the propagation loss of the SP modes, respectively. The real part of n_{eff} and the corresponding

loss are shown in Fig. 9(b) for the example of Al/air/Al structure as a function of the slit widths. We use ε_m = -56.12 + *i*21.01 for aluminum at a wavelength of 633 nm [19]. A phase delay modulation on the surface of a patterned metal film can be realized by simply adjusting the widths of patterned nano-slits. Light focusing can therefore be obtained using a planar structure. The phase delay βd (d is the thickness of the metal film) of the SP modes inside the slits dominates the phase delay distribution across the device surface. For a PL with a focal length f in air, the various slits and their positions can be readily obtained according to the constructive interference principle

$$\beta(x)d + 2\pi\sqrt{f2 + x2}/\lambda = \beta(0)d + 2\pi f/\lambda + 2(m-1)\pi \tag{4}$$

where λ is the wavelength of the illumination, β is a function of the position, and m is the zone number. $\beta(0)$ is the propagation constant of the SP mode in the central slit, which is usually the narrowest slit with the largest value of β. Light coming from slits in a same zone, i.e. a same m (including the case of two identical slits at x and $-x$), has a same phase at the focus. But light from slits in different zones has a phase shift of an integer times of 2π at the focus.

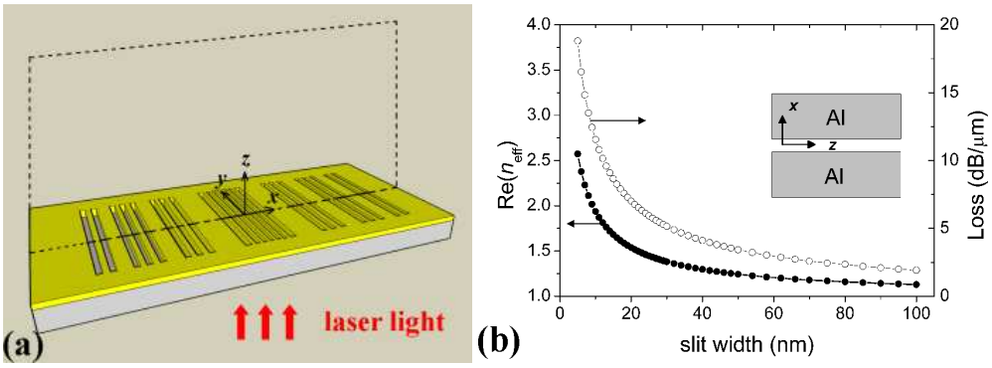

Figure 9. (a) Schematic of a PL. (b) Dependence of the real part of neff and the loss of a SP mode on the slit width. Reprint from [42].

Using Eq. (4), PLs with focal lengths of 0.5 μm, 1 μm, 2 μm, 3 μm, 6 μm and 12 μm at 633 nm were designed in a 200 nm thick aluminium film on a glass substrate. All PLs have an aperture size D of approximately 10 μm. The minimum width of the slit was 10 nm and the minimum gap between two neighboring slits was 50 nm, which was thicker than the skin depth. The central slit, with a width of 10 nm, was at x = 0 and the whole structure was symmetrical in x on the the yz plane. For an ideal planar lens with a focal length f at λ, the phase delay caused by the light path difference is

$$\phi = 2\pi\sqrt{f2 + x2}/\lambda - 2\pi f/\lambda \qquad (x \geq 0) \tag{5}$$

ϕ for each lens calculated from Eq. (5) is shown in Fig. 14 as a solid line. Light emitting from a position at a larger x to the focus has a larger phase delay. By counting from the center we divide the phase delay into zones with a range of 2π. As a result, the slits in a same zone have a same m in Eq. (4). Optimization of the positions and widths of nano-slits gives a

phase delay in the slits of the SP mode, (β(x)*d* - β(0)*d*), obeying the constructive interference principle as shown in Eq. (4). The symbols in Fig. 10 show the phase delay, ϕ', for each slit in different zones. We can see that the symbols and the lines agree very well, i.e. $\phi=\phi'$. For a fixed aperture size, the PL with the longest (shortest) *f* has the smallest (largest) ϕ'_{max}. A PL with a longer focal length has more slits in each zone but has fewer zones. We note that the PL with *f* = 12 μm has almost the same number (21) of slits as the PL with *f* = 0.5 μm that has 22 slits, but the former has 2 zones and the later has 7 zones.

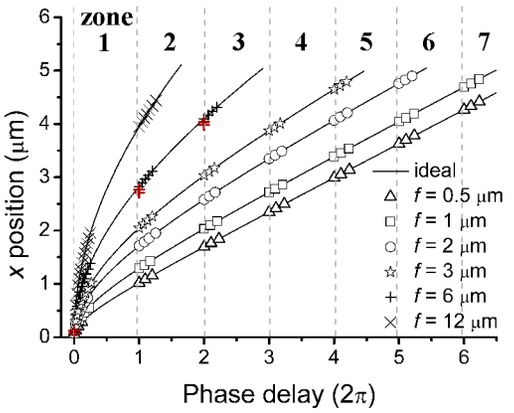

Figure 10. The phase delay ϕ and ϕ′ for each slit in different zones (x ≥ 0) for similar aperture PZPLs with *f* = 0.5 μm, 1 μm, 2 μm, 3 μm, 6 μm and 12 μm at 633 nm. Red crosses are related to the structure shown in Fig. 18(b). Reprint from [42].

4.3. FDTD simulation

A 2D FDTD simulation was chosen to be an adequate approximation since the length of the uniform 10 μm slits in the *y*-direction in our experiment is much larger than the light wavelength. In the simulation, a uniform cell of $\Delta x = \Delta z = 1$ nm was used in the metal slab and a nonuniform cell was used elsewhere. The simulation domain was bounded by perfectly matched layers. A TM-polarized plane wave source at 633 nm was launched with normal incidence to the PL surface from the glass substrate side of the metal film.

4.3.1. PLs with variant focal lengths

The Poynting vector, P_z, distribution of the PL with variant focal lengths is plotted in Fig. 11. As can be seen, P_z for each PL has a light spot at the expected focal point. The constructive interference of the light from each slit at the focus is clearly demonstrated. For the PLs with *f* = 0.5 μm, 1 μm, 2 μm, 3 μm and 6 μm, P_z has its maximum value at the design focus. However, although there is a local maximum in P_z around the design focus for the PL with *f* = 12 μm, the maximum P_z occurs at a distance of 5.4 μm from the PL surface. In [36-39], the shorter focal lengths compared to the designs were explained as a similar phenomenon found in conventional refractive microlens [49]. The effect of diffraction at the lens aperture limits the maximum of the focal length. Using FDTD method, an aperture of 10 μm in the same aluminium film was simulated and showed a peak radiation at a distance of approximately

40 μm. Although the designed focal length of 12 μm is well below this value, the decrease of the focal length still occurs. Furthermore, close examination of the field pattern for the PL with f = 6 μm shows an unwanted local maximum at a distance of 2.1 μm from the PL surface that has an amplitude slightly smaller than that at the focus. Although the PL with f = 12 μm has almost the same number of slits as the PL with f = 0.5 μm in a similar size aperture, the focusing quality of the former is much poorer. The much smaller NA = 0.35 for the PL with f = 12 μm compared to 0.99 for the PL with f = 0.5 μm may be one reason. Furthermore, ϕ'_{max} is 12.5 π for the PL with f = 12 μm and 2.5 π for the PL with f = 0.5 μm.

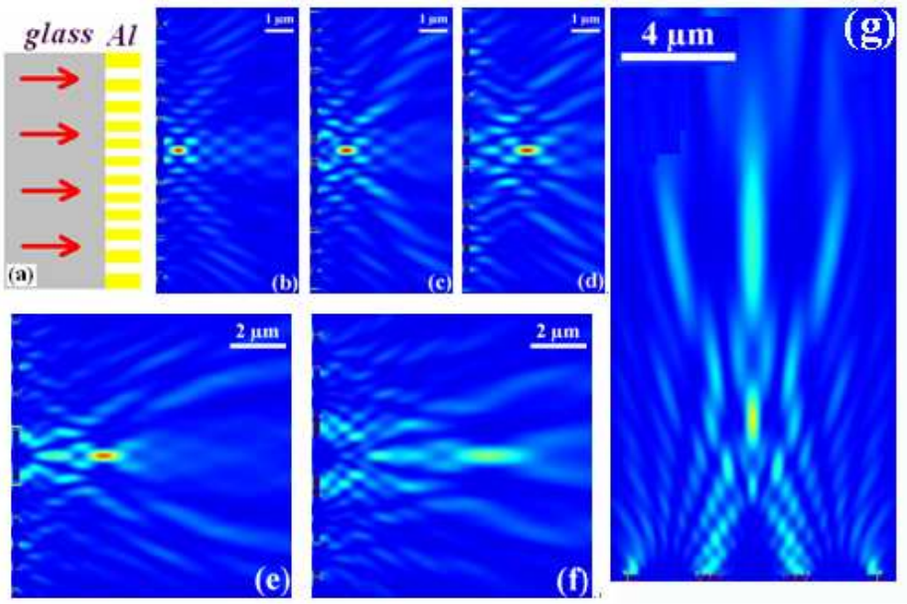

Figure 11. (a) Schematic of the PL. (b)-(g) Simulation results for the Poynting vector Pz distributions of the PZPLs with f = 0.5 μm, 1 μm, 2 μm, 3 μm, 6 μm and 12 μm respectively.

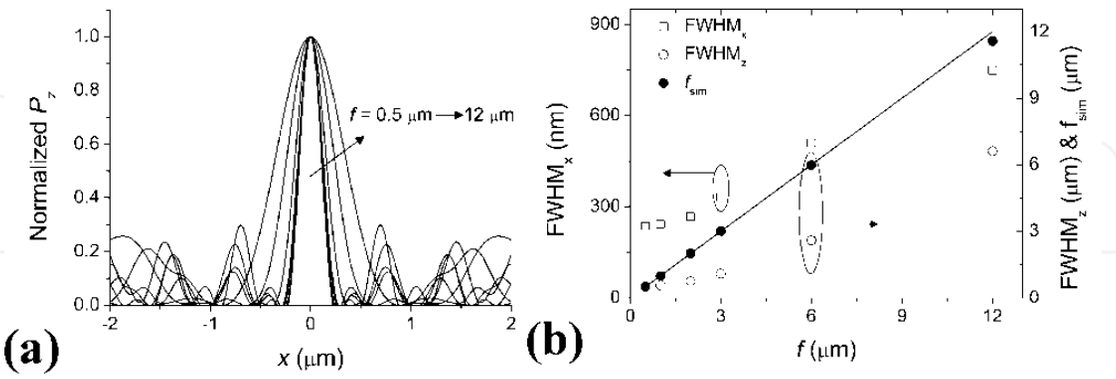

Figure 12. (a) Normalized simulation results for the Poynting vector Pz distributions along the x axis through the foci of PLs with f = 0.5 μm, 1 μm, 2 μm, 3 μm, 6 μm and 12 μm respectively. The optical axis is at x = 0. (b) The simulation results of the focal length, FWHM$_x$ and FWHM$_z$ for PLs with the design f = 0.5 μm, 1 μm, 2 μm, 3 μm, 6 μm and 12 μm respectively. fdesign is plotted as a solid line. Reprint from [42].

In Fig. 12(a) the normalized P_z distribution through the centre of the focus spot along the x axis is shown for each PL in Fig. 11. As can be seen, P_z is tightly confined in the x-direction

although there are some side lobes. The simulation results of the focal length and FWHM of the beam extension in both *x*- and *z*- directions are shown in Fig. 12(b). We can see that the focal length obtained using the FDTD method is in an excellent agreement with the design. Moreover, the FWHM of the beam extension on the *z*-axis ($FWHM_z$) increases with the increasing *f*, starting from 0.49 μm for $f = 0.5$ μm to 6.6 μm for $f = 12$ μm. The FWHM of the beam in the *x*-axis at the focal point ($FWHM_x$) also increases from 236 nm (0.37λ) for $f = 0.5$ μm to 750 nm (1.18λ) for $f = 12$ μm. As a further test of the PL quality, we compared $FWHM_x$ with what we would expect for a diffraction limited beam. The Rayleigh limit for the resolving power of a lens is given by $d_s = \lambda f/D$ for a line, where d_s is the line-width, *D* is the lens aperture and λ is the wavelength. For $f = 6$ μm, the PL has $FWHM_x = 510$ nm while a conventional lens with the same aperture has $d_s = 440$ nm. The PL therefore achieves focus resolution close to the diffraction limit. One advantage of the planar PL is the ability to achieve a large aperture for a small focal length and therefore a high resolution. We would like to mention that the above formula for d_s can not be approximated as $\lambda/2NA$ because *NA* is not even close to $D/2f$ in the case of near-field application. The performance of the proposed plasmonic Fresnel zone plate (FZP), working beyond the diffraction limit in [32], was therefore overestimated.

4.3.2. The effect of the number of zones on the PL performance

Varying the number of zones in the structures, PLs with $f = 0.5$ μm and $f = 6$ μm were simulated. As shown in Fig. 13(a), the simulated focal length has a large deviation from the design for a PL with a small zone number. In the case of a one-zone PL with $f = 6$ μm, *NA* is 0.23 and ϕ'_{max} is 0.5 π. Increasing to three zones, the focal lengths become stable and agree well with the design for both PLs with a focal length approximately 0.8λ and 10λ, respectively. In the case of three zones in the PL with $f = 6$ μm, *NA* is 0.59 and ϕ'_{max} is 4.4 π. The increasing *NA* and ϕ'_{max} provide an accurate focal length as predicted in the design. As shown in Fig. 13(b), the lens aperture ($f = 6$ μm) was found to almost linearly increases with the increasing zone number but $FWHM_x$ reduces. $FWHM_x$ decreases from 510 nm for 3 zones to 258 nm for 16 zones. The resolution approximately doubles at a cost of a 3.3 times increase of the aperture. Although $d_s = \lambda/2NA$ is not valid in the near-field case, the $FWHM_x$ is found to be nearly proportional to $1/NA$, where the trend predicts a resolution of approximately 210 nm at $NA = 1$. So the focal length of a PL agrees with the design very well if the zone number is larger than 3. However, the extension of the focus in the focal plane, i.e. $FWHM_x$, is sensitive to the number of zones. Other authors also found the dependence of the focal lengths of a FZP on the zone numbers [34]. A straightforward understanding is that more zones integrated in the PL aperture, i.e. a larger *NA*, give a focus with a higher contrast because of more constructive light interference from each slit dominates the interference between the diffraction wave from the zones. We should notice that a 3-zone PL with $f = 6$ μm has a same $NA = 0.59$ as a one-zone PL with $f = 0.5$ μm. As can be seen from Fig. 13(a), the accuracy of the focal length of the former is much better than the later. So the number of zones or the total phase shift range of light involving in the interference at the focus is the real factor determining the device performance.

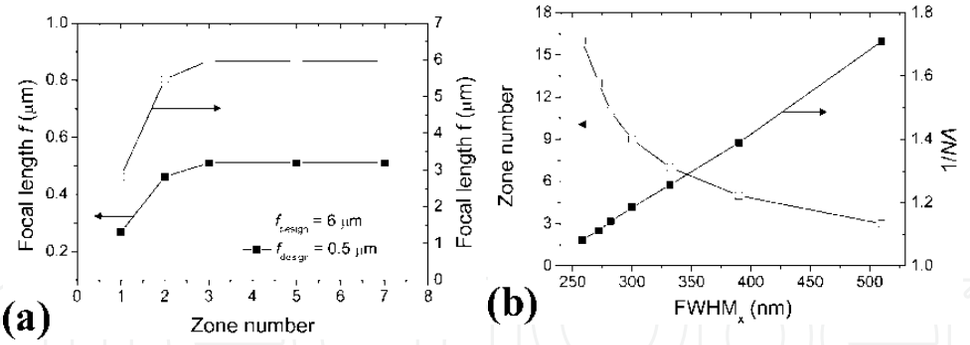

Figure 13. (a) Simulation results for the focal lengths in the PL s with variant zone numbers. The two PLs were designed to have a f of 0.5 μm and 6 μm respectively. (b) Calculated FWHM$_x$ and NA for the PL (f = 6 μm) with variant zone numbers. Reprint from [42].

Simulation results for the Poynting vector P_z distributions of the PL with f = 6 μm and in total 7 zones are shown in Fig. 14(a). Compared to the 3-zone PL shown in Fig. 11(f), the aperture size increases to 15.8 μm from 8.6μm. Accordingly, NA increases from 0.59 to 0.80 and ϕ'_{max} increases from 4.4 π to 12.3 π. The 7-zone PL has a more confined focus both in the focal plane and the light propagating direction. The amplitude ratio to the high-order foci increase as well because the additional zones contribute substantially to the main focus but negligible amount to the high-order foci due to the increasing incline. To achieve a good focusing performance, increasing the lens aperture is a straightforward way. But the footprint increases at the same time. In order to get complete constructive interference at the focus, the amplitude of the diffracted light waves from each zone should be the same. The SP modes in slits with different widths have different loss as shown in Fig. 9(b). Although the phase match at the focus in the design is nearly perfect, the amplitudes of light emitting from each zone are different. Amplitude compensation for the narrow slit is able to balance the constructive interference at the focus and therefore improve the contrast of the focus without increase of the device size. A simple method is proposed to demonstrate this effect as shown in Fig. 14(b), where some additional slits shown as red crosses in Fig. 12 were introduced to the original structure. Two more slits with a width of 10 nm were added neighbouring to each 10 nm slit in the original PL with a gap of 50 nm to enhance the transmitted light contribution at the focus. In this case, both NA and the number of zones are unchanged but very obvious improvement of the contrast around the focus is seen. In addition, the accuracy of the focal length, FWHM$_x$ and FWHM$_z$ are almost the same as the original device.

Although a well-defined focus has been demonstrated above, the transmission efficiency of a PL is still low and the side lobes are obvious. Integrating more slits in a limited lens aperture is a straightforward way to solve this problem. Etching narrower slits in a thicker metal film is one way to integrate more slits due to the increased phase delay across the lens surface but the fabrication is very difficult at a large aspect ratio. The current design has very limited modulation of the phase delay due to the quickly decreasing dependence of the mode propagation constant on the slit width (>30 nm) as shown in Fig. 9(b). Nano-slits narrower than 30 nm are very difficult to fabricate in a thick metal film (>200 nm). The dependence of Re(n_{eff}) on the refractive index of material inside the slits apparently implies a method of phase delay modulation by selectively filled the slits with different materials

[43]. Combining both the slit width and the refractive index tuning, more slits, i.e. a wider phase delay range, can be obtained. The selective refractive index tuning is feasible by applying the masked planarization and the etch-back process.

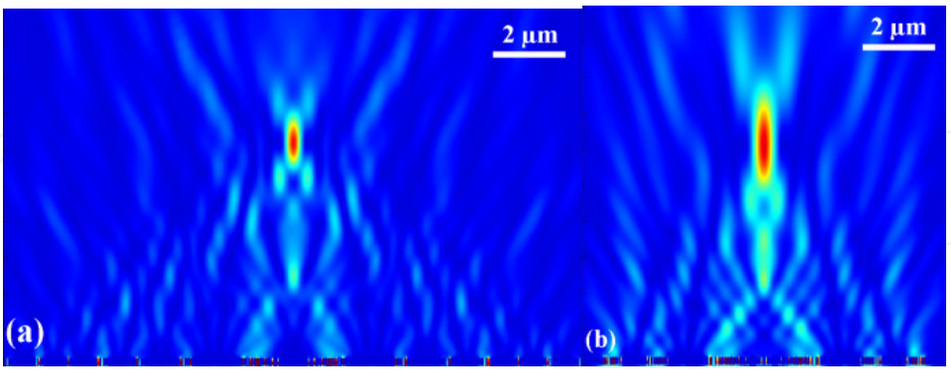

Figure 14. Simulation results for the Poynting vector Pz distributions of the modified structures of the PL shown in Fig. 11(f). (a) A PL with an extended aperture including seven zones compared to three zones in the reference PL. (b) A PL with additional slits shown as red crosses in Fig. 10 compared to the reference PL. Reprint from [42].

4.3.3. Experiments on PLs

The PLs in this work were designed to operate at 633 nm. To simplify the fabrication process, the minimum slit width was 50 nm and the minimum gap was 100 nm in the experiment. Thus the contrast around the focus will degenerate due to the less slits but the accuracy of the focal length keeps in a proper design. Electron beam lithography and dry etch were used to fabricate the nano-slits in a 200 nm thick aluminium film on glass. Fig. 15 shows SEM images of a typical PL structure that was patterned, where the focal length f = 6 μm. The nanoslits were 10 μm in length and the PL width, or aperture, was 10.84 μm. The device has in total 25 slits. From the central slit to the last one on the right hand side, the first four slits have widths of 50 nm, 54 nm, 68 nm, 125 nm and all the others are 100 nm. An enlarged image of the region inside the dash line rectangle of Fig. 15(b) is shown in Fig. 15(c). The roughness on the sidewalls of the gratings is predominantly due to the large grain size of the evaporated aluminium. The error of the slit widths of the fabricated slits is within 10%.

The far-field focusing pattern produced by the lenses was measured using a WITec alpha300S confocal scanning optical microscope (CSOM). A pure confocal mode was used for the experiments because the probe for near-field scanning optical microscopy may have caused a perturbation of the local fields. Sample illumination was with a collimated laser beam operating at 633 nm. The laser source was polarized in the TM mode with its electric field perpendicular to the slits. The light that was transmitted through the sample was collected using a 100×, NA = 0.9 objective. A multi-mode fiber with a core diameter of 25 μm was used to couple the transmitted light into a photomultiplier tube that had a sample integration time is 0.5 ms. The core of the fiber acted as the CSOM pinhole. The sample was scanned in the x and y directions using a piezoelectric scan table, and the microscope working distance was scanned to obtain the z-axis data. The step size in any direction was 200 nm.

Fig. 16(a) and (b) show the focusing light pattern in the *xz* plane measured by the CSOM for lenses designed to have f = 3 μm and f = 6 μm respectively. The diffracted light distribution clearly shows focusing for both lenses. The constructive interference at the focal point can be clearly seen. The positions of the foci and the side lobes agree extremely well with the simulated electric field intensity distribution shown in Fig. 16(c) and (d). The simulation results showed that the field intensity at the focus of the lens with f = 6 μm was 1.9 times that of the incident light. The overall transmission through the lens at 633 nm is 27% that is much larger than the slit filling ratio of 10%. The significant enhancement of the transmission is mainly due to the excitation of SPs [3]. The relatively stronger intensity of the side lobes observed in the experiment was caused by the tolerance limits of fabrication that most strongly affected the narrower slits towards the lens centre. It can be seen that the transmitted light from the central slits is weaker. Theoretical work has also shown that multilayer metal/dielectric films may give a much stronger light intensity at the focus [45].

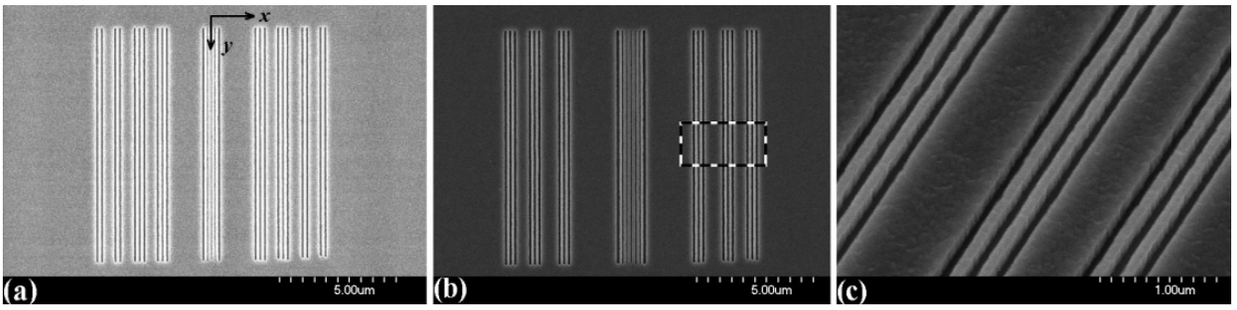

Figure 15. Scanning electron micrographs of PLs in an aluminium film. (a) and (b) are lenses designed to have f = 3 μm and f = 6 μm, respectively. (c) An enlarged image of the region inside the dash rectangle in the tilted PL in (b).

The normalized light intensity distributions through the centre of the focus spot along the *x* and *z* axis, is shown for both lenses in Fig. 17. The experimental focal lengths for the lenses (Fig. 17(a) and (b)) were 3.1 μm and 6.1 μm, which compare favorably with the simulated values of 3 μm and 6 μm, respectively. The deviation from the intended focal length is less than 3.5% for both lenses. The FWHM of the beam extension in the *z*-direction for the lens with a focal length of 3.1 μm is 1.3 μm, and the light intensity at the focus centre is approximately seven times that of the nearest side lobe. The extension of the focus of the lens with the focal length of 6.1 μm is larger as shown in Fig. 17(b). In the *x*-direction, a line plot across the focal plane of each lens shows that the light intensity drops quickly with the distance from the optical axis (at x = 0) as shown in both Fig. 17(c) and (d). The FWHM line-width for the f = 3.1 μm lens is 470 nm, and for the f = 6.1 μm lens it is 490 nm. The resolution of the measured data is potentially limited by the CSOM scan step size of 200 nm and the resolving power of the objective, but as can be clearly seen from Fig. 17, the measured profiles compare very well with the simulations. As a further test of lens quality, we have compared the line-width at the focal point with what we would expect for a Gaussian limited beam. The Rayleigh limit for the resolving power of a lens is given by $d_s = \lambda f/D$, where d_s is a half of the line width, λ is the wavelength, f is the focal length and D is the lens aperture. For the lens with f = 3.1 μm, d_s = 200 nm, whereas for the lens with f = 6.1 μm, d_s = 356 nm. The results therefore suggest that the f = 6.1 μm lens works close to its

theoretical limit. Subdiffraction focusing elements based on near-field effects were reported to be able to focus electromagnetic waves to a spot of size less than $\lambda/10$ [46-48]. However, the focal length is limited to dimensions much less than the wavelength, which is about 100 times less than our devices. Alternatively, we focused on the far-field lenses.

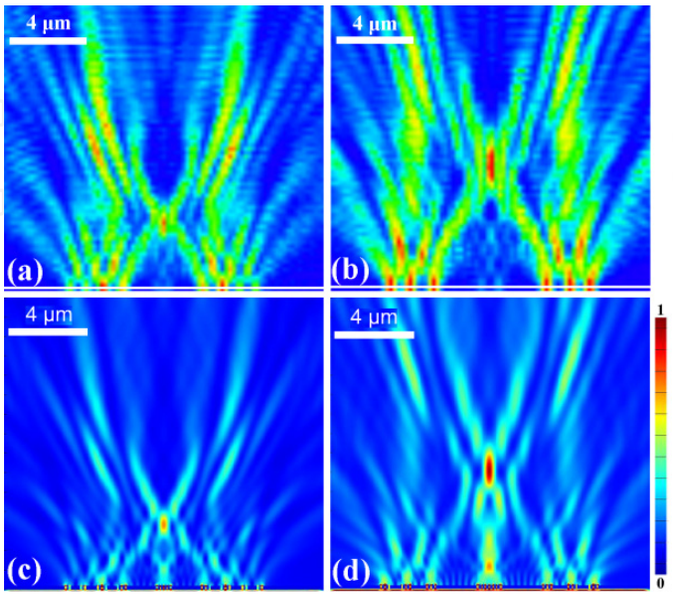

Figure 16. (a) Focusing light pattern in the *xz* plane obtained by the CSOM for a lens designed to have $f = 3$ μm and (b) for a lens designed to have $f = 6$ μm. The horizontal white line in (a) and (b) shows the position of the sample surface. (c) Simulation results for the $f = 3$ μm lens and (d) simulation results for the $f = 6$ μm lens. Reprint from [44].

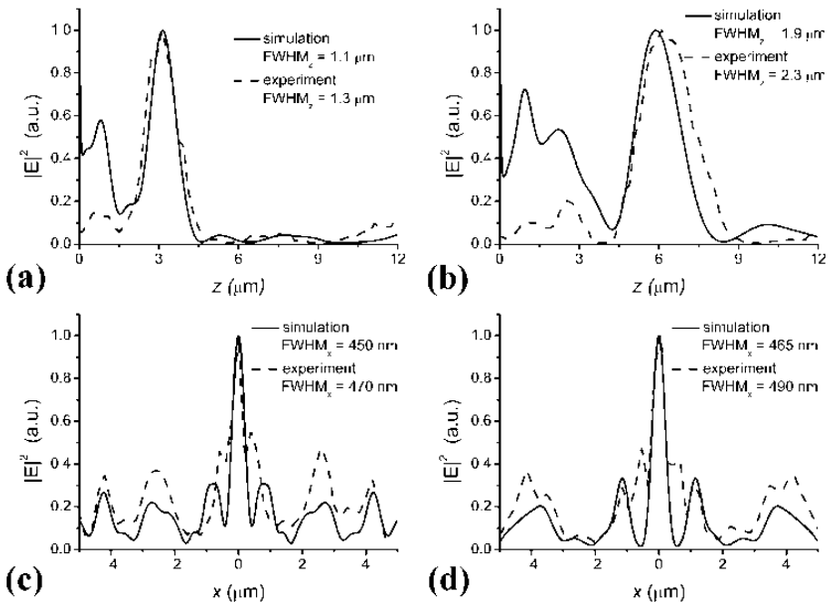

Figure 17. (a) Normalized simulation and experimental results for the light intensity distributions of the lenses. The optical axis is at $x = 0$ and the lens plane is at $z = 0$. (a) and (b) show the distribution along the z direction through the foci of the lenses with $f = 3.1$ μm and $f = 6.1$ μm respectively. (c) and (d) show the distribution along the *x*-direction through the foci of the lenses with $f = 3.1$ μm and $f = 6.1$ μm respectively. Reprint from [44].

To investigate the diffraction effect discussed in Section 4.3, a PL consisting of the central seven slits in the one shown in Fig. 15(b) was fabricated and characterized. As shown in Fig. 18(a), the PL with a single zone shows a light spot far away from the design focus, with an error of 90%. The pattern was also well predicted by the FDTD simulation result as shown in Fig. 18(b). We found that *NA*s are 0.67 and 0.1 and ϕ'_{max} s are 8π and 0.08π for the PLs in Fig. 16(b) and Fig. 18(a), respectively. For a light focusing optical element with the focal length and the aperture size comparable to the wavelength, the number of the zones or ϕ'_{max} play an important role. These experimental results confirm our conclusion that the focal length of a PL is sensitive to the number of zones. More zones give a higher accuracy of the focal length.

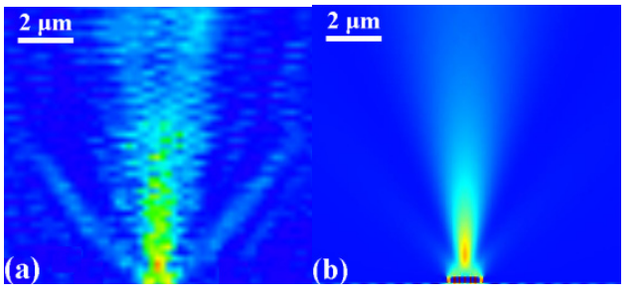

Figure 18. (a) Focusing light pattern in the *xz* plane obtained by the CSOM for a PL consisting of the central seven slits in the one shown in Fig. 15(b). (b) Simulation results for the Poynting vector P_z. Reprint from [44].

5. Plasmonic CMOS image sensors

The above plasmonic optical elements were finally integrated on to CISs. One CIS used in this work has a single-pixel photodiode manufactured with a United Microelectronics Corporation (UMC) 0.18 μm process. The fabrication procedure for pCIS must be modified from that used to make plasmonic filters on glass. To increase the transmission of the colour filters integrated on the CIS, we deposited a layer of SiO_2 on top of the SiN_x surface passivation layer of the CIS before depositing a 150 nm film of aluminium by evaporation. This SiO_2 layer also protected the bond pads of the chip during processing. Before spin-coating with ZEP520A electron beam resist, a thin layer of SiO_2 was added on to the aluminium film to improve adhesion. The sample was exposed using a Vistec VB6 UHR EWF electron beam lithography tool. After development in o-xylene, the sample was etched using CHF_3 and Ar in a Plasmalab 80 plus and then etched using $SiCl_4$ in a Plasmalab System 100. After deposition of a 200 nm thick SiO_2 cap layer, a further mask and etch step was required to reopen windows over the bond-pads of the integrated circuits. Throughout processing the chip was bonded to a Si carrier to aid handling.

As shown in Fig. 19(a)-(c), reflection microscope images of the processed CIS showed different colours of the pixels. The three primary colour filters integrated on the CIS in Fig. 19(a)-(c) were designed to transmit blue (sample S1), green (sample S2) and red (sample S3) light through to the photodiodes. In accordance with this, the reflection spectra showed a complementary minimum in the reflection coefficient for each colour filter. In Fig. 19(c) we

can also see a colour variation across the whole photodiode area. This is caused by non-uniformity in the fabrication of nanohole array. The non-uniformity arose because the CIS was bonded to a carrier using photoresist and there was a non-negligible tilt error during electron beam lithography. As we can see in Fig. 19(c), there are four small slightly different coloured sections in the large pixel area. The boundaries between different sections are the boundaries of the electron beam writing fields between which there is the largest non-uniformity. These non-uniformities would be eliminated in wafer-scale manufacturing.

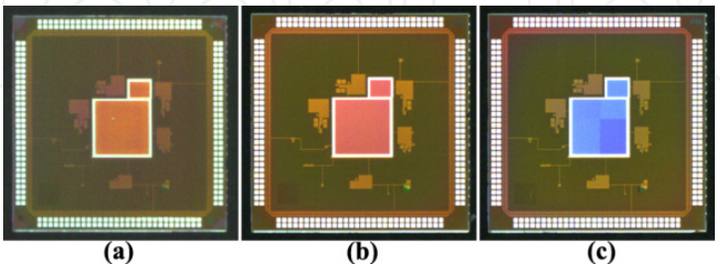

Figure 19. (a)-(c) are microscope images of CIS with integrated blue (S1), green (S2) and red (S3) plasmonic colour filters. Reprint from [49].

Simulated transmission spectra of all three samples are shown in Fig. 20(a). A complete layer stack was modelled using FDTD method to replicate the CIS structure. The stack parameters were derived from the design data of UMC 0.18 μm process. The periods and radiuses are 250nm/80nm, 340nm/90nm and 420nm/110nm for S1, S2 and S3, respectively. Since we could not measure the transmission spectra on the CIS directly, the reflection spectrum was measured instead. The result for sample S2 is shown in Fig. 20(a). As we can see, the experiment and simulation results match very well. The minimum in the reflection coefficient observed in the experimental results is slightly wider than that in simulation. This is mainly caused by the non-uniformity of the nanostructures across the 1 mm^2 photodiode area, as discussed. Photocurrent measurements for the CMOS photodiodes were conducted using a tungsten bulb, a monochromator and an Agilent/HP 4155B. The experimental wavelength resolution of 5 nm was determined by the grating and slit of the monochromator. To test the electrical variations of the photocurrent measurement and themechanical variations of the monochromator, 15 repetitive scans were conducted for one sample; the results showed negligible change. The red dash line in Fig. 20 (b) shows that the photocurrent spectrum of an unprocessed reference CIS has significant fluctuations; most notably two main dips labelled C (520 nm) and D (695 nm). A simple simulation for the whole dielectrics stack using the transfer matrix method showed that the experimental dips approximately match the dips A and B in the simulated spectrum in Fig. 20(b). The dips can be attributed to FP resonances in the CIS dielectric stack. This result is not unexpected since the CMOS process we used has not been optimized, as is usual for commercial CIS. Because we cannot directly measure the transmission spectrum, we have determined the relative transmission using the ratio of the photocurrent for sample S2 to that of an unprocessed reference CIS. The relative transmission spectrum of S2 in Fig. 20(b) has an obvious transmission band for the green colour with an average transmission of approximately 30% and a full-width at half-maximum of 130 nm. There is a sharp

transmission peak near 700 nm that is caused by the shift of the labelled dip D in the photocurrent of S2 due to the change in the stack dielectric structure that arises from our processing as compared to the reference CIS. Optimisation of the CIS dielectric stack would remove this unwanted dip. The relative transmission of CIS S1, S2 and S3 is shown in Fig. 20(c). We can see the transmission bands for blue, green and red respectively. These bands are wider than the simulation results shown in Fig. 20(a). We attribute the poor performance to the non-uniformity of the nanostructures across the whole photodiode area and variation in the fabrication tolerance for the hole sizes required. Note that the unwanted transmission peaks labelled F and G are also a consequence of FP resonances in the unoptimised the unwanted transmission peaks labelled F and G are also a consequence of FP resonances in the unoptimised layer stack. The colour cross talk was evaluated in the same way as a conventional CIS in [50]. Our plasmonic CMOS photodetectors have higher cross talk due to the wider passbands of the fabricated colour filters. But these can be reduced by optimizing the plasmonic filters and the fabrication process. Note that the integration of plasmonic colour filters in a CIS would reduce the colour cross talk between the neighbouring pixels, which is not included in the calculation because the devices discussed here are single-pixel photodetectors.

A CIS with a 100×100-pixel photodiode array was investigated after the initial work on a single-pixel photodetector. As shown in Fig. 21(a), the pixel size is 10 μm × 10 μm and each pixel contains a 4.5 μm × 9 μm photodiode with an inter-photodiode gap of 0.7 μm between some pixels. The topography of the pixels has a 1.1 μm vertical step between the photodiode and the circuit regions within each pixel due to the top metal layer in the AMS 0.35 μm process as shown in Fig. 21(b). Because the CMOS chips use aluminium, it is difficult to register accurately to the pixels using our 100 kV EBL system that has a back-scatter detector. We therefore deposit approximately positioned gold electron beam markers around the CIS using a standard lift-off process. A registration EBL step is then used to write a dummy pattern on to the pixel array. With this pattern we determine the positional error between our gold markers and the pixel array using a high resolution SEM Hitachi S4700 SEM. This data is then used in a third EBL step to write the final pattern on a 150 nm aluminium film evaporated on the photodiode pixel array. Of course, only one lithography step would be needed if this process was implemented in the manufacturing flow of the foundry. A final mask and etch step was required to reopen windows over the bond-pads of the integrated circuits. A microscope image of the processed pixels is shown in Fig. 21(c), where a series of varying plasmonic components were repeated across the photodiode pixel array. In this reflection image it is possible to see the various colours of the pixels due to the SPR generated by differently patterned nanostructures. It is also possible to see black rectangles that correspond to reference pixels, from which the aluminium film above the photodiodes has been totally removed. A SEM image of the pixels with plasmonic filters is shown in Fig. 21(d), where we can see a good alignment of the plasmonic structure to each pixel. The inset in Fig. 21(d) shows a hole array with a period of 230 nm. This filter transmits a dark blue colour.

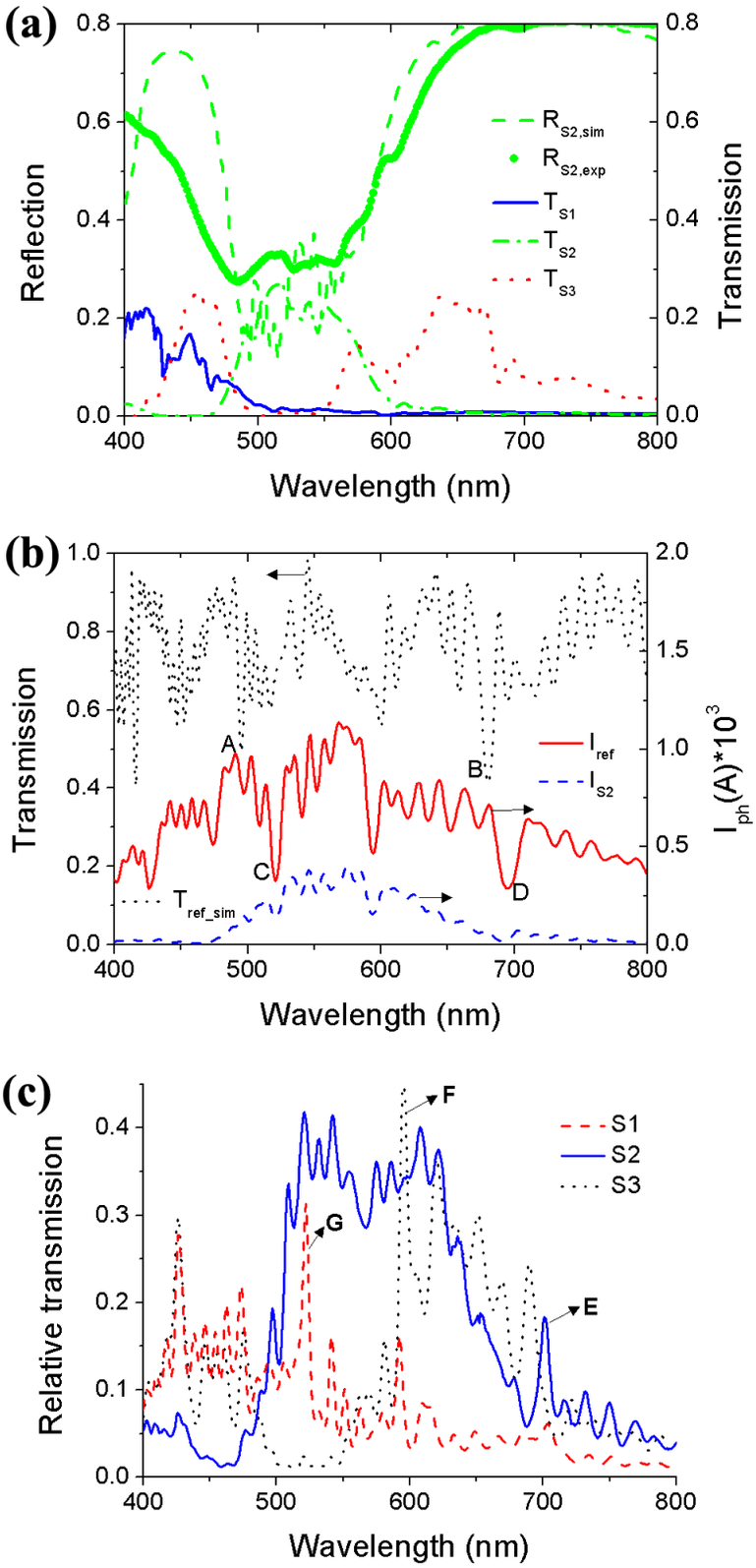

Figure 20. (a) Simulated transmission spectra of CIS S1, S2 and S2. Simulated and measured reflection spectra of S2 are shown as well. (b) Measured photocurrent of the reference sensor and S2. The simulated transmission spectrum of the reference sensor is shown for comparison. (c) Relative transmission of sample S1, S2 and S3. Reprint from [49].

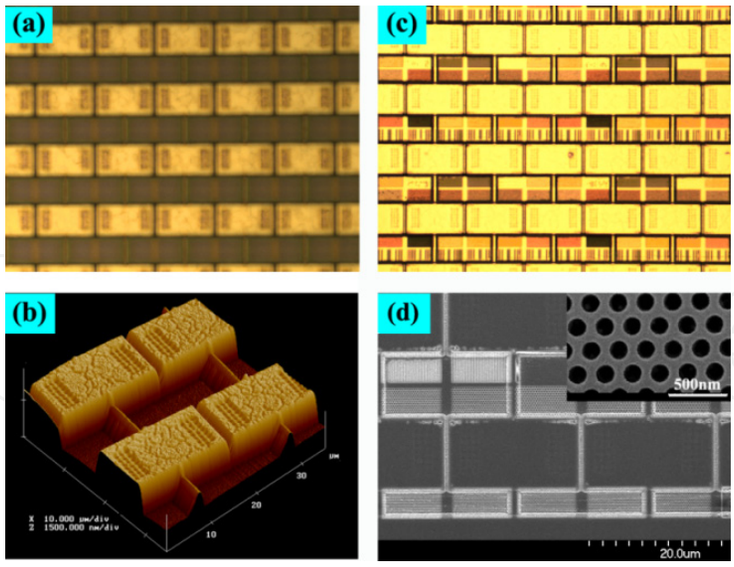

Figure 21. (a) A microscope image of the photodiode pixel array on an unprocessed chip. (b) An AFM image of the topography of pixels before processing. (c) A microscope image of the photodiode pixel array with plasmonic colour filters fabricated on top. (d) A SEM image of the plasmonic colour filters on top of a CIS. The inset is an enlarged image of a filter with the period of 230 nm. Reprint from [21].

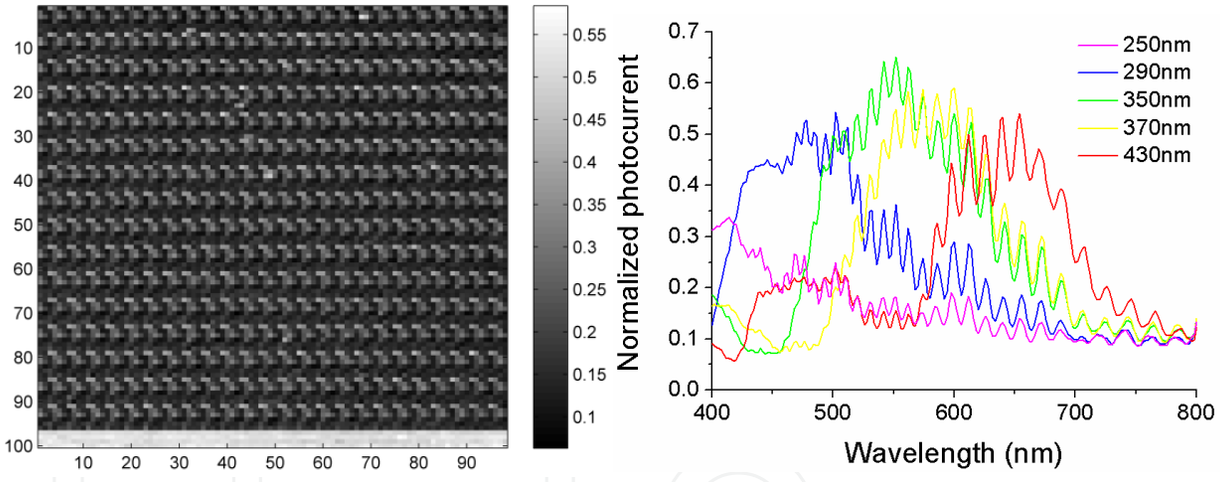

Figure 22. (a) Photocurrent distribution across the 100×100-pixel photodiode array. (b) Normalized photocurrents of photodiodes with various plasmonic colour filters. Reprint from [21].

To test the pixel array, a tungsten bulb and a monochromator were used to illuminate the array with wavelengths in the range between 400 nm and 800 nm. The slits used within the monochromator were chosen to limit the range of wavelengths during each experiment to 5 nm, whilst the centre wavelength was changed in 2 nm increments. At each centre wavelength the response of each pixel, was measured using a data-acquisition system, specifically a NI USB-6218. In order to correct for fixed pattern noise the response of each pixel was determined from the change in the output voltage after an integration time of 125 ms. In addition, to compensate for the effects of the currents that flow within each pixel even in the absence of light, the response of each pixel after an integration time of 125 ms in the absence of light was subtracted from the response at each centre wavelength. The

response distribution across the pixel array when it is illuminated by light with a wavelength of 550 nm is shown in Fig. 22(a) to demonstrate that, with the exception of a very few defective pixels, there is a good uniformity to the plasmonic components. The spectral responses we present have been determined by averaging the responses of all the pixels with the same plasmonic filter, across the whole pixel array. Since it is impossible to directly measure the transmission spectrum of the filters, the performance of the filters has been assessed by normalizing the average response of each pixel design using the average response of the unpatterned reference pixels. Results for pixels with five different plasmonic filters (Fig. 22(b)), show that the filters act as bandpass filters with different centre wavelengths. The normalized responses of these filters are above 50% of the signal measured from an unprocessed pixel and the FWHMs are between 110 nm and 150 nm. One obvious feature of these results that was not seen in the results in Fig. 4(c) is the oscillations in all the responses. The fact that these oscillations were previously observed in the single-pixel plasmonic CMOS photodetector and that they are also observed in the responses of pixels before any back end of line processing has occurred leads to the conclusion that they are attributable to FP resonances in the CIS dielectric stack. The resonances occur because the layers in the dielectric stack have different permittivities, hence there is a reflection at each interface. This result is not unexpected since the CMOS process we used has not been optimised to reduce this effect, as is usual for commercial CIS.

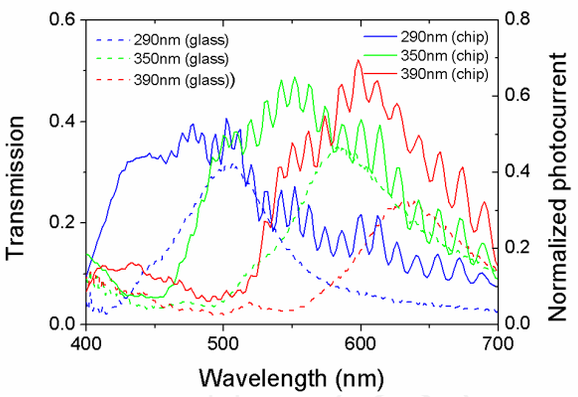

Figure 23. Normalized photocurrents of three sets of photodiodes with peak responses close to 445 nm, 555 nm and 600 nm. Transmission spectra of the same colour filters on glass are shown for comparison. Reprint from [21].

Average results of three groups of pixels with the peak response wavelengths close to Red (600 nm), Green (555 nm), Blue (445 nm), according to the 1931 International Commission on Illumination 2° standard observer colour matching functions [51], are shown in Fig. 23. The transmission spectra of the same filters on glass are shown for comparison. All photodiode pixels show a blue-shift of their peak responses compared to the peak transmission wavelengths of the plasmonic colour filters on glass. Two factors contribute to this phenomenon; one is the smaller hole sizes of the filters integrated on chip than those on glass, the other is the high-index substrate loading effect in the case of CMOS chips. This effect can be eliminated by calibration of the process for colour matching. In addition the transmission

bands of the filters on the CIS seem to be wider than the equivalent filters when they are made on glass. The phenomena that could be contributed to this broadening include the possibility that a wider range of angles of incidence of light occur when the pixels are tested and cross-talk caused by the large vertical separation, 8 μm, between the filters and the photodiodes underneath. These effects mean that the results obtained are not necessarily representative of those that will be obtained in an optimized manufacturing process, especially if the plasmonic colour filters are integrated in lower metal layers in a standard CMOS process. In addition, it is anticipated that the broadening will be reduced by using narrow band filters such as low loss silver filters. The optoelectronic efficiency can be further improved if these plasmonic nanostructures are fabricated close enough to the photodiodes, where the localized field can be greatly enhanced due to the SPR effects [52]. It is anticipated that in future state-of-the-art CMOS technology (ITRS roadmap 2010) the half-pitch in Metal 1 will scale down to 32 nm in 2012, enabling mass manufacture of suitable SPR structures.

6. Conclusion

We demonstrated a detailed study of plasmonic optical elements for the application in CISs and the first plasmonic CIS with plasmonic colour filters replacing conventional polymer colour filter array. The plasmonic optical elements such as colour filters, polarizers and lenses showed promising performance where the complete control on wavelength filtering, polarization and the phase distribution were achieved by carefully optimizing the metallic nanostructures. The complete compatibility with the CMOS technology of these metallic optical devices facilitates the plasmonic CIS integration. Replacing the conventional optical elements, plasmonic devices offer various advantages such as less cross-talk, low cost and multifunction, etc. It would be an important step forward to apply nanophotonics in the CMOS imaging. It could be a new way to bring plasmonics research from the lab to the foundry.

Author details

Qin Chen
Corresponding Author
Suzhou Institute of Nano-Tech and Nano-Bionics, Chinese Academy of Sciences, China
University of Glasgow, United Kingdom
SOC Key Laboratory, Peking University Shenzhen Research Institute, China

Xiaohua Shi
Suzhou Institute of Nano-Tech and Nano-Bionics, Chinese Academy of Sciences, China

Yong Ma
University of Glasgow, United Kingdom

Jin He
Peking University Shenzhen SOC Key Laboratory, PKU-HKUST Shenzhen-Hongkong Institution, Shenzhen, P.R. China

7. References

[1] Raether H. Surface Plasmons. Berlin: Springer; 1988.

[2] Gramotnev DK, Bozhevolnyi SI. Plasmonics beyond the diffraction limit. Nature Photonics 2010;4 83-91.

[3] Ghaemi HF, Thio T, Grupp DE, Ebbesen TW, Lezec HJ. Surface plasmons enhance optical transmission through subwavelength holes. Physical Review B 1998;58 6779-6782.

[4] Genet C, Ebbesen TW. Light in tiny holes. Nature 2007;445 39-46.

[5] Laux E, Genet C, Skauli T, Ebbesen TW. Plasmonic photon sorters for spectral and polarimetric imaging. Nature Photonics 2008;2 161-164.

[6] Xu T, Du C, Wang C, Luo X. Subwavelength imaging by metallic slab lens with nanoslits. Applied Physics Letters 2007;91 201501.

[7] Verslegers L, Catrysse PB, Yu Z, Fan S. Planar metallic nanoscale slit lenses for angle compensation. Applied Physics Letters 2009;95 071112.

[8] Koo C, Kim H, Paik K, Park D, Lee K, Park Y, Moon C, Lee S, Hwang S, Lee D, Kong J. Improvement of crosstalk on 5M CMOS image sensor with 1.7x1.7μm² pixels. In Proc. Of SPIE 2007;6471 647115.

[9] Prima J, Roy F, Leininger H, Cowache C, Vaillant J, Pinzelli L, Benoit D, Moussy N, Giffard B. Improved colour separation for a backside illuminated image sensor with 1.4 μm pixel pitch. Proc. International Image Sensor Workshop, Bergen, Norway; 2009.

[10] Catrysse PB, Wandell BA. Integrated colour pixels in 0.18um complementary metal oxide semiconductor technology. Journal of the Optical Society of America A 2003;20 2293-2306.

[11] Catrysse PB. Monolithic integration of electronics and sub-wavelength metal optics in deep submicron CMOS technology. Materials Research Society Symposium Proceedings 2005;869 D1.5.1-D1.5.12.

[12] Kanamori Y, Shimono M, Hane K. Fabrication of transmission color filters using silicon subwavelength gratings on quartz substrates. IEEE Photonic Technology Letters 2006;18 2126-2128.

[13] Collin S, Vincent G, Haidar R, Bardou N, Rommeluere S, Pelouard J. Nearly perfect Fano transmission resonances through nanoslits drilled in a metallic membrane. Physical Review Letters 2010;104 027401.

[14] Xu T, Wu Y, Luo X, Guo LJ. Plasmonic nanoresonators for high-resolution colour filtering and spectral imaging. Nature Communications 2010;1 59.

[15] Inaba Y, Kasano M, Tanaka K, Yamaguchi T. Degradation-free MOS image sensor with photonic crystal colour filter. IEEE Electron Device Letters 2006;27 457-459.

[16] Frey L, Parrein P, Raby J, Pellé C, Hérault D, Marty M, Michailos J. Color filters including infrared cut-off integrated on CMOS image sensor. Optics Express 2011;19 13073-13080.

[17] Lee HS, Yoon YT, Lee SS, Kim SH, Lee KD. Colour filter based on a subwavelength patterned metal grating. Optics Express 2007;15 15457-15463.

[18] Lumerical FDTD Solution, http://www.lumerical.com/

[19] Walls K, Chen Q, Collins S, Cumming DRS, Drysdale TD. Automated design, fabrication and characterization of colour matching plasmonic filters. IEEE Photonics Technology Letters 2012;24 602-604.
[20] Chen Q, Cumming DRS. High transmission and low colour cross-talk plasmonic colour filters using triangular-lattice hole arrays in aluminium films. Optics Express 2010;18 14056-14060.
[21] Chen Q, Das D, Chitnis D, Walls K, Drysdale TD, Collins S, Cumming DRS. A CMOS Image Sensor Integrated with Plasmonic Colour Filters. Plasmonics, DOI: 10.1007/s11468-012-9360-6.
[22] Andreou AG, Kalayjian ZK. Polarization imaging: principles and integrated polarimeters. IEEE Sensors Journal 2002;2 566-576.
[23] Schechner YY, Narasimhan SG, Nayar SK. Polarization-based vision through haze. Applied Optics 2003;42 511-525.
[24] Tokuda T, Sato S, Yamada H, Ohta J. Polarization analyzing CMOS sensor for microchamber/microfluidic system based on image sensor technology. IEEE International Symposium on Circuit and Systems, May 18-21, 2008, Seattle, USA.
[25] Zhao X, Boussaid F, Bermak A, Chigrinov VG. Thin Photo-Patterned Micropolarizer Array for CMOS Image Sensors. IEEE Photonics Technology Letters 2009;21 805-807.
[26] Nordin GP, Meier JT, Deguzman PC, Jones MW. Micropolarizer array for infrared imaging polarimetry. Journal of the Optical Society of America A 1999;16 1168-1174.
[27] Ekinci Y, Solak HH, David C, Sigg H. Bilayer Al wire-grids as broadband and high-performance polarizers. Optics Express 2006;14 2323-2334.
[28] Huo Y, Fesenmaier CC, Catrysse PB. Microlens performance limits in sub-2μm pixel CMOS image sensors. Optics Express 2010;18 5861-5872.
[29] Lezec HJ, Degiron A, Devaux E, Linke RA, Martin-Moreno L, Garcia-Vidal FJ, Ebbesen TW. Beaming Light from a Subwavelength Aperture. Science 2002;297 820-822.
[30] Sun Z, Kim HK, Refractive transmission of light and beam shaping with metallic nano-optic lenses Applied Physics Letters 2004;85 642-644.
[31] Shi H, Wang C, Du C, Luo X, Dong X, Gao H. Beam manipulating by metallic nano-slits with variant widths. Optics Express 2005;13 6815-6820.
[32] Fu Y, Zhou W, Lim L, Du CL, Luo XG. Plasmonic microzone plate: Superfocusing at visible regime. Applied Physics Letters 2007;91 061124.
[33] Chen Y, Zhou C, Luo XG, Du C. Structured lens formed by a 2D square hole array in a metallic film. Optics Letters 2008;33 753-755.
[34] Mote RG, Yu SF, Ng BK, Zhou W, Lau SP. Near-field focusing properties of zone plates in visible regime - New insights. Optics Express 2008;16 9554-9564.
[35] Verslegers L, Catrysse PB, Yu Z, Shin W, Ruan Z, Fan S. Phase front design with metallic pillar arrays. Optics Letters 2010;35 844-846.
[36] Verslegers L, Catrysse PB, Yu Z, White JS, Barnard ES, Brongersma ML, Fan S. Planar Lenses Based on Nanoscale Slit Arrays in a Metallic Film. Nano Letters 2009;9 235-238.
[37] Lin L, Goh XM, McGuinness LP, Roberts A. Plasmonic Lenses Formed by Two-Dimensional Nanometric Cross-Shaped Aperture Arrays for Fresnel-Region Focusing. Nano Letters 2010;10 1936-1940.

[38] Fu Y, Liu Y, Zhou X, Xu Z, Fang F. Experimental investigation of superfocusing of plasmonic lens with chirped circular nanoslits. Optics Express 2010;18 3438-3443.
[39] Goh XM, Lin L, Roberts A. Planar focusing elements using spatially varying near-resonant aperture arrays. Optics Express 2010;18 11683-11688.
[40] Ruffieux P, Scharf T, Herzig HP, Völkel R, Weoble KJ. On the chromatic aberration of microlenses. Optics Express 2006;14 4687-4694.
[41] Gordon R, Brolo AG. Increased cut-off wavelength for a subwavelength hole in a real metal. Optics Express 2005;13 1933-1938.
[42] Chen Q. Effect of the Number of Zones in a One-Dimensional Plasmonic Zone Plate Lens: Simulation and Experiment. Plasmonics 2011;6 75-82.
[43] Chen Q. A novel plasmonic zone plate lens based on nano-slits with refractive index modulation. Plasmonics 2011; 6 381-385.
[44] Chen Q, Cumming DRS. Visible light focusing demonstrated by plasmonic lenses based on nano-slits in an aluminum film. Optics Express 2010;18 14788-14793.
[45] Kim HC, Ko H, Cheng M. High efficient optical focusing of a zone plate composed of metal/dielectric multilayer. Optics Express 2009;17 3078-3083.
[46] Grbic A, Jiang L, Merlin R. Near-Field Plates: Subdiffraction Focusing with Patterned Surfaces. Science 2008;320 511-513.
[47] Eleftheriades GV, Wong AMH. Holography-Inspired Screens for Sub-Wavelength Focusing in the Near Field. IEEE Microwave and Wireless Components Letters 2008;18 236-238.
[48] Gordon R. Proposal for Superfocusing at Visible Wavelengths Using Radiationless Interference of a Plasmonic Array. Physical Review Letters 2009;102 207402.
[49] Chen Q, Chitnis D, Walls K, Drysdale TD, Collins S, Cumming DRS. CMOS Photo Detectors Integrated with Plasmonic Colour Filters. IEEE Photonic Technology Letters 2012;24 197-199.
[50] Agranov G, Berezin V, Tsai RH. Crosstalk and microlens study in a color CMOS image sensor. IEEE Transactions on Electron Devices 2003;50 4-11.
[51] CIE Free Documents for Download: CIE 1931 Standard Colorimetric Observer Data. http://www.cie.co.at/main/freepubs.html.
[52] Schaadt DM, Feng B, Yu ET. Enhanced semiconductor optical absorption via surface plasmon excitation in metal naonparticles. Applied Physics Letters 2005;86 063106.